# $\pi$ bonding versus electronic-defect generation: An examination of band-gap properties in amorphous carbon

U. Stephan, Th. Frauenheim, P. Blaudeck, and G. Jungnickel
*Department of Physics, Technical University of Chemnitz-Zwickau, D-09009 Chemnitz, PSF 964, Germany*
(Received 20 January 1994)

The electronic properties of amorphous carbon structures with varying microscopic mass densities, ranging from 2.0 to 3.52 g/cm$^3$, are analyzed. Using a semiempirical density-functional approach the model structures were generated by molecular dynamics performing a simulated cooling of liquid carbon clusters, containing 128 atoms, within periodically arranged cubic supercells. By investigation of properties related to chemical bonding we find a strong control of the band gap by the balance between $\pi$ bonding and electronic defect generation. As important sources that influence the $\pi - \pi^*$ band gap the distance distribution between non-$\sigma$-bonded hybrid orbitals as well as the topological properties of clustering $sp^2$ (or $sp$) units are discussed. A number of local densities of states are calculated at representative atoms to validate the classification of $\pi$ clusters and electronic defect states used.

## I. INTRODUCTION

The deposition of amorphous carbon ($a$-C) is stimulating a still increasing number of research activities. It opens new perspectives in thin film science and technology due to the wide variability in the mechanical, optical, and electronic properties. Stable tetrahedral forms of hydrogen-free amorphous carbon, $ta$-C, recently have been grown by filtered vacuum arc evaporation and mass-selected ion beam deposition.[1–5] These materials have been demonstrated to behave like semiconductors with relatively large band gaps.[6] They have been successfully doped,[7,8] a fact that considerably stimulates effort in using $ta$-C to make devices[7–9] and to understand the structure-related electronic properties on the level of chemical bonding and $\pi$-cluster formation.

Although many current activities are concerned with obtaining knowledge about structure-formation mechanisms of amorphous carbon, the electronic band-gap properties of these materials are still controversially discussed throughout the literature.[10–17] In particular, since 1987 the gap-closing mechanisms in the low-density modifications have been related to Robertson and O'Reilly's $\pi$-bonding cluster model.[18] Their argument was based on the fact that optical band-gap values in $a$-C(:H) are often quite small compared to the Hückel $\pi - \pi^*$ gap in basic $\pi$ systems such as ethylene and benzene. A possible conclusion was straightforward in searching for gap-closing sources from aromatic clustering. The argumentation widely accepted so far has explained the band-gap variation in differently prepared $a$-C materials by the various extent of planar graphitic clusters mainly including even-membered rings. These ideas have stimulated a lot on how to look on amorphous carbon structures, but they never have been founded on a quantitative theoretical calculation based on atomic-scale microstructures.

Recently, Robertson reexamined his $\pi$-bonding aromatic cluster model of amorphous carbon in reducing the average size of clusters that are considered to be responsible for small electronic band gaps in $a$-C materials.[19] Galli *et al.*,[12] using self-consistent field (SCF) density-functional (DF) molecular-dynamics (MD) methods, report on graphitelike arrangements of "thick planes" formed by five-, six-, and seven-membered rings, where the $sp^2$ atoms tend to lie nearly on the same plane. Wang *et al.*,[16] by means of empirical tight-binding MD, again claim to find graphitelike sheets which consist of six- and a few five- and seven-membered rings. In this way these two investigations seem to support the cluster model discussed by Robertson and O'Reilly.[18] Various $a$-C structures obtained by classical empirical potentials, on the other hand, have to be characterized as electronically unstable.[20,21] This is due to the neglect of an additional structure stabilizing $\pi$-bonding interaction thus producing a random distribution of $sp^2$ and $sp^3$ sites and a nearly uniform dihedral-angle distribution of neighboring non-$\sigma$-bonded hybrid orbitals.[21] In contrast to the Galli and Wang results Frauenheim *et al.*[14] report on $a$-C microstructures of varying mass density that are formed by almost equal portions of five-, six-, and seven-membered rings which are puckered and strongly cross linked due to the inclusion of $sp^3$ atoms in most of these rings. Substantial aromatic clustering causing larger portions of $sp^2$ sites to arrange in plane under the constraint of the rigid network in the small supercell clusters has not been found for any mass density. Pronounced $\pi - \pi^*$ gaps, however, have been obtained for almost all densities, thus indicating that any argumentation treating aromatic clusters as the origin of $\pi - \pi^*$ gaps need not necessarily be true. In other terms, these results, which are based on a quantitative theoretical model, contradict the widespread use of the aforementioned aromatic-cluster arguments.

To further clear up discussions on sources affecting band-gap widening or closing in amorphous carbon materials this paper presents a quantitative analysis of $a$-C microstructural models generated by a semiempirical MD DF annealing simulation,[14] including model systems

for highly tetrahedral high-density *ta*-C modifications. To reduce the influence of the small supercell size on the structural evolution as well as to better account for medium-range order effects, the simulations have been performed by using 128-atom supercell clusters having twice the volume of the cells considered previously.[14]

After discussing relevant structural data in comparison with previous *a*-C simulations we focus on electronic structure calculations in *a*-C models generated at different mass densities. The band-gap behavior as characterized by the gap width, the ratio of $\pi$ and $\sigma$ bonds, and the distribution of $\pi$ states and defects will be related to the nature of $\pi$-bonded clusters (size, topology, and degree of relaxation of $\pi$ bonds). From this analysis we show that undercoordinated atoms form chainlike or ramified $\pi$ clusters which only seldom contain aromatic rings. With increasing mass density the cluster size reduces, giving rise to a preferred constitution of $\pi$-bonded pairs or slightly larger even-membered $\pi$ clusters. As the result, in the modifications with 3.0 and 3.3 g/cm$^3$ the smaller-clustered $\pi$ bonds are strengthened, implying an optimum reduction of stress from the rigid $sp^3$ matrix and an opening of the $\pi - \pi^*$ gap [defined as the separation between the highest occupied and the lowest unoccupied $\pi$-like molecular orbitals (HOMO-LUMO)] of about 3 eV. The effect of hydrogen incorporation during the MD simulations will be the subject of a related paper[22] in which evidence is given for a further stress reduction in the high-density hydrogenated analogs leading to an additional increase of the band gap above 3 eV.

The outline of the paper is as follows. In Sec. II we briefly discuss the theoretical method and the simulation regime used for the MD and verify its applicability to the problems of interest. The structural properties of the different *a*-C modifications in relation to experimental thin film studies are analyzed in Sec. III. On the basis of a local orbital description a method for investigating the local $\pi$-bonding properties and the electronic defects in *a*-C structures is outlined in Sec. IV. Related to the electronic density of states (DOS) behavior this serves as the basis for achieving a deeper insight into the electronic band-gap properties of amorphous carbon materials in Sec. V. In Sec. VI, before summarizing, we discuss a number of local densities of states calculated at representative atoms to validate the classification of $\pi$ clusters and electronic-defect states used.

## II. MD STRUCTURE SIMULATION

To model the structure formation in amorphous carbon modifications we have carried out MD simulations for 128 carbon atoms using fixed-volume cubic supercell arrangements of varying size in relation to the microscopic mass densities to be studied. The structures have been generated by the application of identical simulated annealing conditions, performing a quenching of a partly equilibrated liquid structure over a total annealing time of $4 \times 10^{-12}$ s. Due to the constant atom number per supercell the cohesive energies for different densities have been compared directly, thus yielding the most stable structure under the given set of simulation conditions as that which has the lowest energy.

The method which was outlined previously as a semiempirical DF approach for MD (Ref. 14) includes first-principle concepts in relating the Kohn-Sham orbitals of the atomic configuration to a minimal basis of the localized atomiclike valence orbitals of all atoms, which along with the single atomic potentials are determined self-consistently within the local-density approximation. Each valence orbital is represented by a set of 12 Slater-type functions. Making use of a simplified non-self-consistent DF scheme for the many-atom configuration the effective one-electron potential in the Kohn-Sham Hamiltonian is approximated as a sum of potentials of neutral atoms. Consistent with this approximation one can neglect several contributions to the Hamiltonian matrix elements in the secular equation leaving a simplified general eigenvalue problem for determining the cluster electron eigenvalues and wave functions[23,24]: $\sum_\mu c_\mu^i (h_{\mu\nu} - \varepsilon_i S_{\mu\nu}) = 0$. The total energy of the system as a function of the atomic coordinates can now be decomposed into two parts, $E_{\rm tot}(\{\mathbf{R}_l\}) = E_{\rm bind}(\{\mathbf{R}_l\}) + E_{\rm rep}(\{\mathbf{R}_l - \mathbf{R}_k\})$. The first term appearing as the sum over all occupied cluster electron energies represents the so-called band-structure energy, and the second, as an repulsive energy, comprises the core-core repulsion between the atoms and interactions between electrons at different lattice sites that partly compensate. As a further approximation this repulsive energy is modeled by short-range repulsive empirical two-particle potentials (polynomials of fifth order) which are fitted to best reproducing the potential energy curves of the corresponding two-atomic molecules in dependence on a wide range of the interatomic separation ($\geq 1.3 a_B$, where $a_B$ is the Bohr radius). This procedure, already applied for the study of stability and structure-related properties of *a*-C(:H),[14] improves the fitting scheme reported earlier,[13] where the first attempts were made in simply reproducing the two-atomic equilibrium separations and the experimental vibrational frequencies. Related to the carbon-carbon interaction a time step of 80 atu (1 atu = $2.4 \times 10^{-17}$ s) was found to be sufficient for handling the Verlet algorithm and to guarantee the conservation of energy during the simulation run.

Upon numerous computational tests, the method has proven to model a representative number of carbon structures quantitatively correct. Carbon microclusters,[13] fullerenes,[25] bulk-crystalline modifications, and diamond surfaces[26] have been investigated, reproducing experimentally found structures. Moreover, the relative differences of the cohesive energy per carbon atom as a function of structure and coordination closely approximate results obtained by more sophisticated methods (SCF DF, SCF Hartree-Fock). As an important outcome the method accounts well for the $\pi$-bonding effects which are characteristic in the carbon chemistry.

## III. STRUCTURAL PROPERTIES

As the result of the simulation we have obtained final metastable *a*-C configurations of varying microscopic mass densities between 2.0 and 3.52 g/cm$^3$. As the most

TABLE I. Electronic properties of the $a$-C model structures. $\Delta E$/atom, total energy difference per atom related to the minimal-energy structure (in eV); $E_\pi^{\mathrm{LUMO}} - E_\pi^{\mathrm{HOMO}}$, separation between bonding and antibonding $\pi$ states (in eV); $\pi$ pairs/$N_\pi$, total number of free orbitals contained in two-atomic $\pi$ clusters related to all bonding and antibonding $\pi$ states.

| Density | 2.0 | 2.2 | 2.4 | 2.7 | 3.0 | 3.3 | 3.52 |
|---|---|---|---|---|---|---|---|
| $\Delta E$/atom | 0.858 | 0.642 | 0.525 | 0.380 | 0.164 | 0.091 | 0.0 |
| $E_\pi^{\mathrm{LUMO}} - E_\pi^{\mathrm{HOMO}}$ | 1.93 | 1.87 | 2.23 | 2.26 | 2.88 | 2.98 | 5.56 |
| $\pi$ pairs/$N_\pi$ | 0.197 | 0.188 | 0.118 | 0.303 | 0.667 | 0.692 | 0.250 |

stable structures under the constraint of a fixed supercell volume the high-density modifications with 3.0 g/cm$^3$ and larger have the lowest energies containing 64% up to 88% of carbon atoms within an $sp^3$ bonding configuration. In particular the 3.0 g/cm$^3$ structure has been found to have a very low defect density along with a $\pi$–$\pi^*$ HOMO-LUMO band gap of 2.9 eV (cf. first two rows of Table I).

The high-density modifications determined as the most stable structures represent a material which has been formed under nonequilibrium conditions controlling the evolution of a very dense low-energy atomic configuration. Similar structures have been grown recently by filtered vacuum arc evaporation and mass-selected ion-beam deposition.[1–5] In both cases high fractions of $sp^3$ bonded atoms controlled by the density are obtained in agreement with the theoretical modeling. Though we are still far away from a realistic simulation of deposition processes, the quenched amorphous carbon structures describe relevant structural (diffraction) and electronic properties determined experimentally on low- and high-density $a$-C modifications quantitatively well.[27,28] In Table II some characteristic structural data are summarized for all models considered. For a comparison, some recent experimental and theoretical results are cited in Table III. Computer-assisted images of the most of the structures which provide a further impression of the structural properties of our models are given in Fig. 1, where differently coordinated atoms have been represented in green and blue color.

There is a clear tendency of promoting enlarged fractions of $sp^3$ bonded atoms by a controlled increase of the microscopic mass density that drives the character of clustering to change considerably. In the low-density metastable structures of 2.0 and 2.2 g/cm$^3$ a formation of homogeneous dense networks will not be achieved. One obtains density fluctuations including $sp$-like hybridized chain segments that interlink more dense clusters of puckered five-, six-, and seven-membered rings incorporating a high $sp^2$ fraction, but also a number of $sp^3$ atoms. The $sp^2$ clustering is additionally stabilized by $\pi$-bonding

TABLE II. Structural data for theoretically derived amorphous carbon modifications $a$-C in dependence on the mass density. (C2,C3,C4, content of twofold, threefold, and fourfold coordinated atoms; $R1$, mean nearest-neighbor distance; $\Theta$, mean bond angle; $k_{\mathrm{CC}}$, total CC coordination number).

| Density (g/cm$^3$) | C2 (%) | C3 (%) | C4 (%) | $R_1$ (Å) | $\Theta$ (deg) | $k_{\mathrm{CC}}$ |
|---|---|---|---|---|---|---|
| 2.0 | 27 | 64 | 9 | 1.43 | 120.6 | 2.80 |
| 2.2 | 14 | 69 | 17 | 1.47 | 117.0 | 3.03 |
| 2.4 | 7 | 70 | 23 | 1.48 | 115.4 | 3.16 |
| 2.7 | 3 | 53 | 44 | 1.52 | 112.8 | 3.41 |
| 3.0 | | 36 | 64 | 1.54 | 111.1 | 3.64 |
| 3.3 | | 25 | 75 | 1.53 | 110.4 | 3.75 |
| 3.52 | | 12 | 88 | 1.54 | 109.6 | 3.88 |

TABLE III. Structural data for theoretically and experimentally derived amorphous carbon structures, taken from the literature. The meaning of the symbols is the same as in Table II.

| Density (g/cm$^3$) | C2 (%) | C3 (%) | C4 (%) | $R_1$ (Å) | $\Theta$ (deg) | $k_{\mathrm{CC}}$ |
|---|---|---|---|---|---|---|
| theoretical relaxations | | | | | | |
| 2.0[a] | | 85 | 15 | 1.44 | | 3.20 |
| 2.2[b] | 12.0 | 80.6 | 7.4 | | | 2.96 |
| 2.44[b] | 5.8 | 80.0 | 14.2 | | | 3.08 |
| 2.69[b] | 6.5 | 71.0 | 22.5 | | | 3.16 |
| 2.0[c] | | | 10 | 1.47 | 118.7 | 3.1 |
| 2.9[c] | | | 25 | 1.48 | 116.7 | 3.25 |
| 3.2[c] | | | 70 | 1.53 | 110.7 | 3.7 |
| 2.0[d] | 13 | 80 | 7 | 1.50 | 117.9 | 2.93 |
| 2.5[d] | 5 | 79 | 16 | 1.49 | 115.9 | 3.05 |
| 3.0[d] | 1 | 65 | 34 | 1.51 | 113.6 | 3.33 |
| experimental structures | | | | | | |
| 1.8[e] | | | 10 | 1.43 | | 3.0 |
| 2.1[e] | | | 10 | 1.44 | | 3.2 |
| 2.44[f] | | | 6.4 | 1.46 | 117 | 3.34 |
| 3.0[g] | | | 55 | 1.51 | 115.2 | 3.4 |
| 3.0[g] | | | 65 | 1.52 | 113.3 | 3.3 |
| 2.9[h] | | | 92 | 1.53 | 110 | 3.7 |

[a]Reference 12.
[b]Reference 16.
[c]Reference 15.
[d]Reference 20.
[e]Reference 29.
[f]Reference 30. Given $a$-C network density from the radial distribution function, density from weighting samples: 2.0 g/cm$^3$.
[g]Reference 28.
[h]Reference 2.

cluster formation, which for the lowest-density structure percolates through the system. The extent of the $\pi$-bonded clusters will be analyzed in more detail in Sec. V. But already now it should be noted that the number of completely $\pi$-bonded rings, given in comparison with the total number of rings in Table IV, is very low even in the lowest-density structures. Increasing the density up to 2.4 and 2.7 g/cm$^3$ the $sp$-like sites disappear. These structures may be characterized as a relatively homogeneous distribution of smaller groups of $sp^2$ and $sp^3$ atoms creating puckered ring clusters that are strongly cross linked to generate the amorphous network. In rising the density further to 3.0 and 3.3 g/cm$^3$ and finally to the diamond value, $a$-C forms a predominantly tetrahedrally coordinated homogeneous $sp^3$ matrix including randomly distributed $sp^2$ atoms, which preferentially are paired. The electronic consequences of this structural behavior are again postponed until Sec. V.

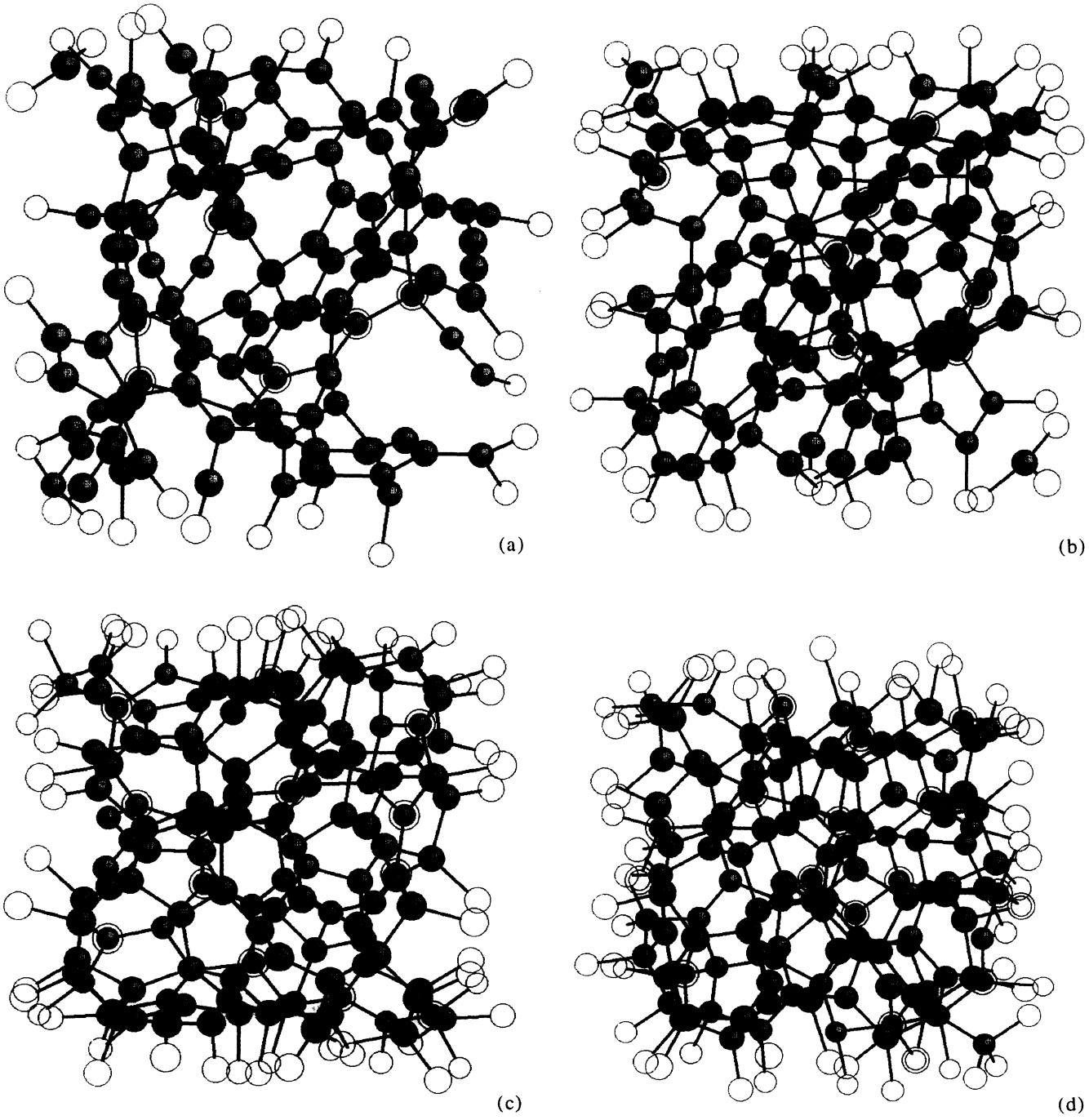


FIG. 1. Computer images of $a$-C supercell structures with variation of mass density: 2.0 (a), 2.4 (b), 2.7 (c), 3.0 (d), 3.3 (e), and 3.52 g/cm$^3$ (f). Green spheres denote twofold and threefold coordinated atoms, blue spheres denote fourfold ones. Open circles refer to atoms in the neighboring supercells. For convenience (e) and (f) have been enlarged as compared with the first ones by a factor of 65/60.

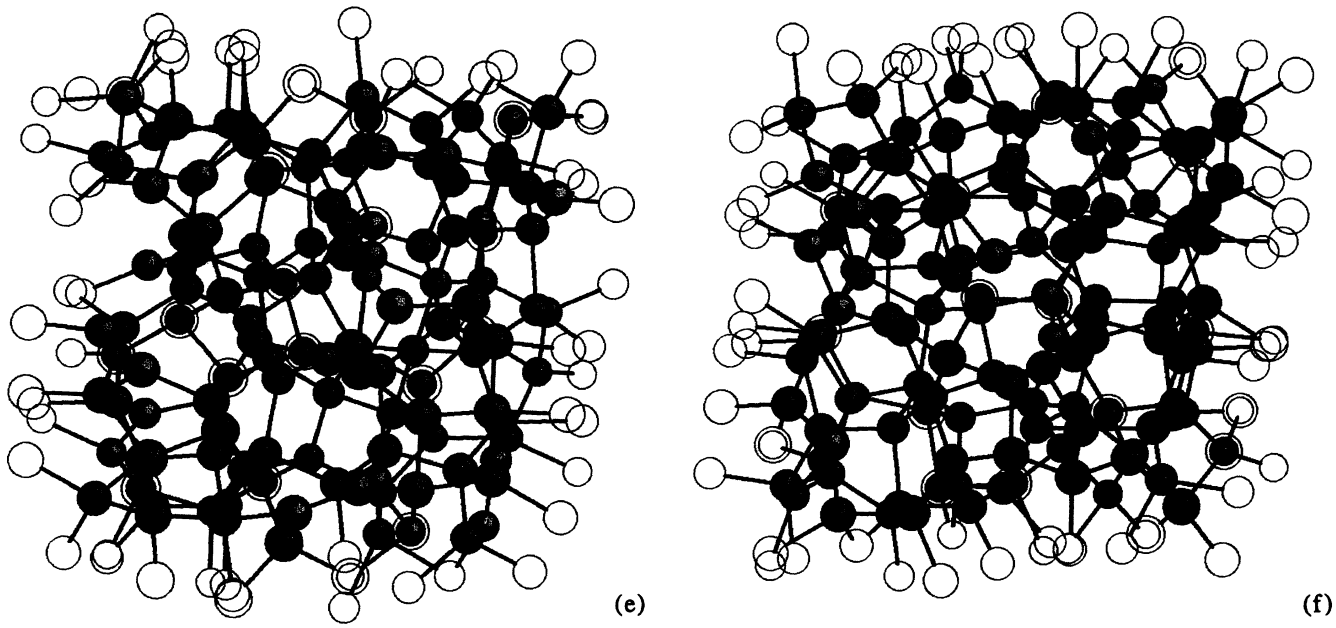


FIG. 1 *(Continued).*

The changes in the bonding properties as a function of density variation are illustrated by the bond-length histograms in Fig. 2, showing the distribution of various types of bonds in different grey shading. Furthermore, the fractions of the bonds between equally coordinated carbon atoms are additionally presented in this figure. (Hereafter, two-, three-, and fourfold coordinated carbon atoms are referred to as C2, C3, and C4 atoms, respectively, the cutoff radius for this classification being 1.85 Å.)

The models having densities up to 2.4 g/cm$^3$ contain a number of C2 atoms, which as a result of $\pi$ interaction form some "triplelike" bonds with bond lengths of about 1.23 Å. With increasing density these atoms vanish, whereas the number of C4 sites grows thus producing bonds with lengths of about 1.55 Å. This fact is reflected by a global shift of the total bond-length distribution to larger distances. The number of bonds between C3 neighbors remains, however, relatively constant for the low-density models, inferring the change in the network connectivity to be mainly determined by a competition between the reduction of C2-C2 bonds and the emergence of C4-C4 bonds. In the high-density modifications with-

TABLE IV. Total and $\pi$-bonding ring statistics of $a$-C models calculated via a shortest-path ring analysis, and reference values for graphite and diamond.

| Density (g/cm$^3$) | arbitrary/$\pi$-bonded rings 4 | 5 | 6 | 7 |
|---|---|---|---|---|
| 2.0 | 1/0 | 9/1 | 5/2 | 8/0 |
| 2.2 | 1/0 | 12/1 | 14/2 | 14/1 |
| 2.4 | 1/0 | 22/2 | 20/1 | 11/0 |
| 2.7 | 3/0 | 24/0 | 36/1 | 26/0 |
| 3.0 | 6/0 | 36/0 | 54/0 | 32/0 |
| 3.3 | 5/0 | 39/0 | 60.0 | 54.0 |
| 3.52 | 5/0 | 41/0 | 79/0 | 67/9 |
| graphite | 0/0 | 0/0 | 64/64 | 0.0 |
| diamond | 0/0 | 0/0 | 256/0 | 0/0 |

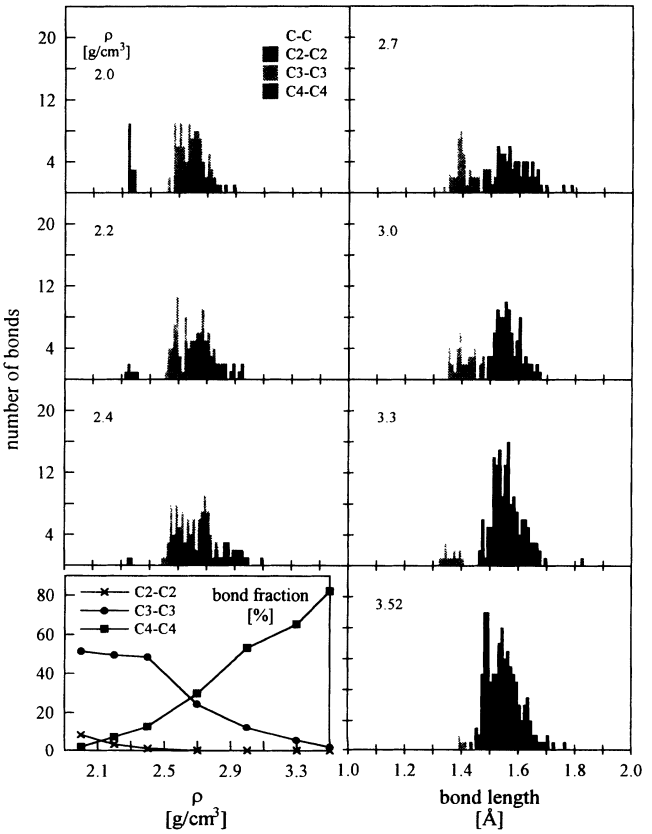


FIG. 2. Bond-length histograms of $a$-C models with different mass densities $\rho$. Furthermore, the fractions of C2-C2, C3-C3, and C4-C4 bonds related to all bonds within the models are also shown.

out C2-C2 bonds the further increase of the density gives rise to a roughly linear increase of the number of C4-C4 bonds and a strong reduction of the number of C3-C3 bonds. It should be noted that the standard deviation of the total bond-length distribution is found to be nearly constant at a value of 0.08 Å for the whole range of densities between 2.0 and 3.0 g/cm$^3$ and decreases slightly for densities above 3.0 g/cm$^3$.

Now let us consider the clustering tendencies within our models from a purely statistical point of view. To this end, we have calculated the partial coordination numbers[22] for differently coordinated carbon atoms. These values may be compared with the corresponding numbers for systems of the same chemical composition and density, but with a random distribution of different hybrids. This distribution is characterized by the requirement that the probability for one atom to be in a certain hybridization state is independent of the hybridization states of the neighboring atoms. Equally hybridized atoms of such systems are only able to cluster by statistical reasons. The partial numbers $k_{ij}$ are calculated as the number of C$j$ atoms neighboring an atom C$i$, related to all C$i$ atoms. As given in Table V, the single-component coordination numbers $k_{22}$, $k_{33}$, and $k_{44}$ clearly exceed the values of the random distribution whereas the mixed numbers are found to be smaller than the corresponding ones of the random case. This fact demonstrates that atoms of the same hybridization state tend to cluster for all densities considered.

For a comparison of our results with other simulations reported in the literature, comprising (1) fully SCF *ab initio* MD methods,[12] (2) empirical tight-binding MD methods,[16] as well as (3) Monte Carlo (MC) and MD simulated-annealing (SA) calculations based on the classical empirical Tersoff potential,[15,20] the structural data of correspondingly generated $a$-C models have been included in Table III.

The *ab initio* results of Galli *et al.*[12] for the low-density $a$-C structure show similar chemical bonding properties as the 2.0 g/cm$^3$ structure analyzed in this paper. The fractions of about 15% $sp^3$ and 85% $sp^2$ bonded atoms, obtained by these authors, may be related to an interpretation of experimental data on $a$-C films prepared by evaporation or sputtering,[12] but contrast with the considerable fraction of 27% C2 atoms found in our 2.0 g/cm$^3$ model. (The possible origin of these differences has been discussed in Ref. 16.) Moreover, the graphitelike arrangements of "thick planes" formed by coupled five-, six-, and seven-membered rings in the structure of Galli cannot be confirmed by our simulations. We find several coupled ring clusters including similar portions of five-, six-, and seven-membered rings which are cross linked and puckered due to the inclusion of $sp^3$ atoms in most of these rings.

The occurrence of C2 atoms in a similar order of magnitude has also been reported by Wang *et al.*[16] using semiempirical tight-binding MD simulations. In their analysis, they again find extended $\pi$-bonded regions of sizes of about 10 Å × 10 Å, which they call graphitelike sheets. These regions contain mostly six- and some five- and seven-membered rings and are bridged by C2 and C4 atoms. The fractions of $sp^3$-bonded atoms obtained from Wang's structures are, on the other hand, by a factor of about 2 lower than the C4 values found in our studies. The deviations observed should be related to the different approximation schemes starting from a first-principles ansatz here and an empirical tight-binding parametrization in Wang's paper. These approaches are expected to work differently if structure formation processes are concerned where configurations far from equilibrium geometries have to be evaluated.

For making the comparison more complete we have also included structural data derived on the basis of the empirical Tersoff potential using a MC algorithm in the constant pressure-temperature $(N,P,T)$ ensemble[15] as well as MD SA studies within the $(N,V,E)$ ensemble.[20] Kelires[15] reports on three characteristic modifications. In the 2.0 g/cm$^3$ modification designated as $e$-C (evaporated $a$-C) the threefold bonding geometry predominates. The topology may only locally be characterized as graphite-

TABLE V. Partial coordination numbers for the $a$-C models and for the corresponding random distribution structures (denoted as rnd) with given mass density (in g/cm$^3$) and equal composition of differently coordinated atoms.

| Model | | $k_{ii}$ | | | $k_{ij}$ $(i \neq j)$ | | | | | |
|---|---|---|---|---|---|---|---|---|---|---|
| | | $k_{22}$ | $k_{33}$ | $k_{44}$ | $k_{23}$ | $k_{24}$ | $k_{32}$ | $k_{34}$ | $k_{42}$ | $k_{43}$ |
| 2.0 | $a$-C | 0.86 | 2.24 | 0.55 | 0.89 | 0.20 | 0.38 | 0.38 | 0.64 | 2.82 |
| | rnd | 0.39 | 2.06 | 0.49 | 1.37 | 0.25 | 0.59 | 0.37 | 0.78 | 2.75 |
| 2.2 | $a$-C | 0.67 | 2.18 | 1.27 | 1.00 | 0.33 | 0.20 | 0.61 | 0.27 | 2.45 |
| | rnd | 0.19 | 2.04 | 0.91 | 1.36 | 0.45 | 0.28 | 0.68 | 0.37 | 2.72 |
| 2.4 | $a$-C | 0.44 | 2.18 | 1.79 | 1.33 | 0.22 | 0.13 | 0.69 | 0.07 | 2.14 |
| | rnd | 0.09 | 2.00 | 1.15 | 1.34 | 0.57 | 0.13 | 0.86 | 0.18 | 2.67 |
| 2.7 | $a$-C | 0.00 | 1.56 | 2.32 | 1.50 | 0.50 | 0.09 | 1.35 | 0.04 | 1.64 |
| | rnd | 0.04 | 1.40 | 2.06 | 0.94 | 1.03 | 0.06 | 1.54 | 0.07 | 1.87 |
| 3.0 | $a$-C | | 1.26 | 3.02 | | | | 1.74 | | 0.98 |
| | rnd | | 0.89 | 2.82 | | | | 2.11 | | 1.18 |
| 3.3 | $a$-C | | 0.81 | 3.27 | | | | 2.19 | | 0.73 |
| | rnd | | 0.60 | 3.20 | | | | 2.40 | | 0.80 |
| 3.52 | $a$-C | | 0.50 | 3.64 | | | | 2.50 | | 0.36 |
| | rnd | | 0.29 | 3.61 | | | | 2.71 | | 0.39 |

like controlled by a random distribution of nonplanar $sp^2$ sites without significant medium-range correlations. This is opposed to our results in which the structural behavior and clustering is controlled by the strong $\pi$-bonding nature of the network driving differently bonded atoms to cluster and $sp^2$ sites to align each other. A $\pi$-like interaction that depends on the angle between free orbitals, however, is completely missing in the Tersoff concept.[20] In the case of the high-density modification of 3.2 g/cm$^3$ the Tersoff potential seems to model the overall behavior of $a$-C structures more realistically. A more detailed comparison of clustering including correlations to the electronic properties for the structures of Kelires has been made by Lee *et al.*[21]

An analysis of the electronic properties of MD generated Tersoff-based $a$-C structures by Stephan and Haase[20] supports the results of Kelires and proves the reliability of Tersoff's concept to realistic simulations of amorphous carbon by means of electronic structure (DOS) calculations. All the MD simulated structures comprising the high-density modifications show a strong predominance of trigonal $sp^2$ bonded atoms. For the high-density system (3.0 g/cm$^3$) this is in contradiction with recent experimental findings[2,6,28] and with our results,[14] but there is some agreement with the annealed $i$-C* structure of Kelires (2.9 g/cm$^3$; cf. Table III). As a consequence of the neglect of $\pi$-bonding angular terms, the $\pi$ bonds and $\pi$-bonded clusters are only created at random, hence distinct defect bands emerge near the Fermi energy $E_F$. This situation counteracts the physically realistic adjustment of an electronically minimized energy configuration. It has been shown[20] how these bands arise from the unsaturated and uncorrelated atomic orbitals. The weight of these bands decreases unambiguously with decreasing number of the defects, i.e., with increasing mass density. Owing to the large number of defects, all Tersoff-relaxed structures have to be considered as electronically unstable. These problems may only be tackled by a proper treatment of undercoordinated atoms, which is a sophisticated task within an empirical-potential framework,[31] but is naturally included in *ab initio* type simulations.

## IV. π BONDING ANALYSIS

To obtain a more profound knowledge about the structure of $\pi$-bonded clusters in our models as well as on correlations between structural and electronic properties we have developed a simplified $\pi$-bonding analysis. Recently,[20] this procedure was first applied to structures produced by MD using the empirical potential of Tersoff. The main features of the method are as follows.

The first step is to transform the original linear combination of atomic orbitals (LCAO) basis of $s$ and $p$ atomiclike valence orbitals to the local basis of orthonormal hybrid orbitals which are directed to the nearest-neighbor atoms. Then for C3 and C2 atoms one obtains free, i.e., non-$\sigma$-bonded, orbitals which can be classified according to their $p$ characters. This is done in Table VI using a minimum value of 93% for hybrid orbitals to be denoted as $p$-like. (This value is also suitable to distinguish between $sp$- and $sp^2$-like C2 atoms.) Free orbitals that fall below this value are referred to as $sp^x$ ones.

Table VI shows the majority of the free hybrids in all structures to be predominantly $p$-like, which is the consequence of the fact that the mean bond angle of C3 atoms equals a value near 120°, whereas C2 atoms tend to become stretched. Both classes of orbitals are treated equivalently, but it should be kept in mind that the free $sp^x$ hybrids in general produce eigenstates which have somewhat lower energy compared with the $p$-like ones. Having defined the hybrid states of the atoms, two undercoordinated atoms may be considered as $\pi$-like bonded if the overlap integral of their free hybrids exceeds a critical value necessary to create a significant minimum in the local density of states (LDOS) at an isolated pair of $sp^2$ atoms (0.042 chosen for our LCAO parameters). In the case of C2 atoms the maximum possible hybrid overlap is used.

Unlike previously,[20] we have included in our analysis the weak $\sigma$-like interactions of C3 (or C2) atoms which have a somewhat too large separation (> 1.8 Å) from each other to form an ordinary bond, but exhibit an interaction strength comparable with $\pi$ bonds. Such weak or stretched bonds have extensively been discussed for many years in the investigation of $a$-Si(:H) (see, e.g., Refs. 32–34). The occurrence of carbon atoms which form weaker bonds (thus becoming fourfold coordinated atoms including this bond) was recently examined by Kelires.[15] Because the corresponding atomic distances in our case belong to a region around a minimum in the radial distribution function, these bonds in general affect the electronic properties of our structures only slightly. For the higher-density structures, however, their influ-

TABLE VI. Number of different kinds of free atomic orbitals and nonbonding $\pi$ states (related to one atom), and fraction of the nonbonding to the bonding and antibonding $\pi$ states ($n_p/n_{p+\pi}$) as well as of all $\pi$ states to the $\sigma$ states ($n_{p+\pi}/n_\sigma$).

| Density (g/cm$^3$) | Non-$\sigma$-bonded orbitals | | | Unbonded orbitals | Nonbonding $\pi$ states | $\frac{n_p}{n_\pi}$ | $\frac{n_{p+\pi}}{n_\sigma}$ |
|---|---|---|---|---|---|---|---|
| | $p$ | $sp^x$ | sum | | | | |
| 2.0 | 1.047 | 0.102 | 1.203 | 0.039 | 0.086 | 0.077 | 0.430 |
| 2.2 | 0.852 | 0.117 | 0.969 | 0.031 | 0.055 | 0.060 | 0.320 |
| 2.4 | 0.719 | 0.125 | 0.844 | 0.008 | 0.047 | 0.059 | 0.267 |
| 2.7 | 0.508 | 0.086 | 0.594 | 0.063 | 0.078 | 0.152 | 0.174 |
| 3.0 | 0.305 | 0.086 | 0.391 | 0.000 | 0.031 | 0.087 | 0.108 |
| 3.3 | 0.211 | 0.055 | 0.266 | 0.047 | 0.047 | 0.214 | 0.071 |
| 3.52 | 0.078 | 0.047 | 0.125 | 0.039 | 0.063 | 1.000 | 0.032 |

ence proved to be non-negligible (cf. Sec. V).

The $\pi$ bonds defined in this way are used to establish $\pi$-bonded clusters of atoms. The size and topology of the clusters may now be investigated. Furthermore, it is straightforward to proceed with an estimation of the nonbonding $\pi$ states near $E_F$. Note that the correct distribution of the nondiagonal Hamiltonian matrix elements in some cases (e.g., odd-membered chains) has no influence on the number of the nonbonding states, and in other cases this influence is roughly described by the chosen threshold overlap value. (This means that the critical overlap requires a compromise between the residual interactions below this value and the smaller separations of bonding/antibonding states for larger clusters.) On the other hand, the eigenvalues of the nonbonding states are relatively unsensitive to the exact overlap nearest-neighbor matrix elements. We therefore apply a procedure which is similar to a simple Hückel theory. First, the nonbonding states are considered to include all unbonded atomic orbitals, i.e., orbitals that do not contribute to any $\sigma$ or $\pi$ bond. These orbitals produce defect states which are to be denoted as isolated defects. We then perform an analysis of the nearest-neighbor bonding matrices of all $\pi$-bonded clusters including more than two atoms. The ranks of these matrices provide the number of nonbonding states to the eigenvalue $E = 0$. Hence these states may appropriately be referred to as topological defects. By calculating the ratio of all defect states to the remaining bonding and antibonding $\pi$ states, cf. Table VI, a coarse estimate of the shape of the TDOS near $E_F$ can be inferred.

## V. ELECTRONIC PROPERTIES

The electronic properties of the relaxed structures may first of all be characterized by their total densities of electronic states (TDOS). For a comparison, in Fig. 3 we give the results of two methods for the TDOS calculation. The first is a Gaussian smoothing of the LCAO eigenvalue spectrum obtained via a simple $\Gamma$-point approximation of the cluster eigenfunctions which then have the full periodicity of the supercell structure (solid lines). The second procedure is the Haydock recursion method[35] (dashed lines), which for the used length of the continued fraction (40 levels) approximates a full integration over the first Brillouin zone using effectively 719 up to 1331 special **k** points[36,37] for the lower- and higher-density structures, respectively. The $s$ and $p$ partial TDOS as well as the summed TDOS can now be obtained from a summation over various (in our case 15) recursion runs using randomly chosen initial recursion vectors which are restricted to the desired orbital types.[38] The correct summation to the TDOS has been ensured by a Löwdin orthonormalization of the atomiclike basis orbitals. In this recursion case, the smoothing has been done by means of the Gaussian quadrature method.[39]

Both methods agree very well except for the low valence-band edge where some spurious peaks appear in the recursion DOS and for the $\sigma$ conduction band where in the LCAO diagonalization case a number of plane waves have additionally been used to improve the high-energy part of the TDOS.[13] The LCAO $\Gamma$-point method has therefore proven to be correct for the used number of atoms in our supercells. The agreement, however, becomes less satisfactory in the low-energy part of the $\sigma$ valence DOS for the high-density structures. For these models the applied supercell occupies its smallest volume and the evolution of sufficiently extended recursion orbitals into Bloch functions requires even more **k** values.

In the following, let us discuss the calculated TDOS,

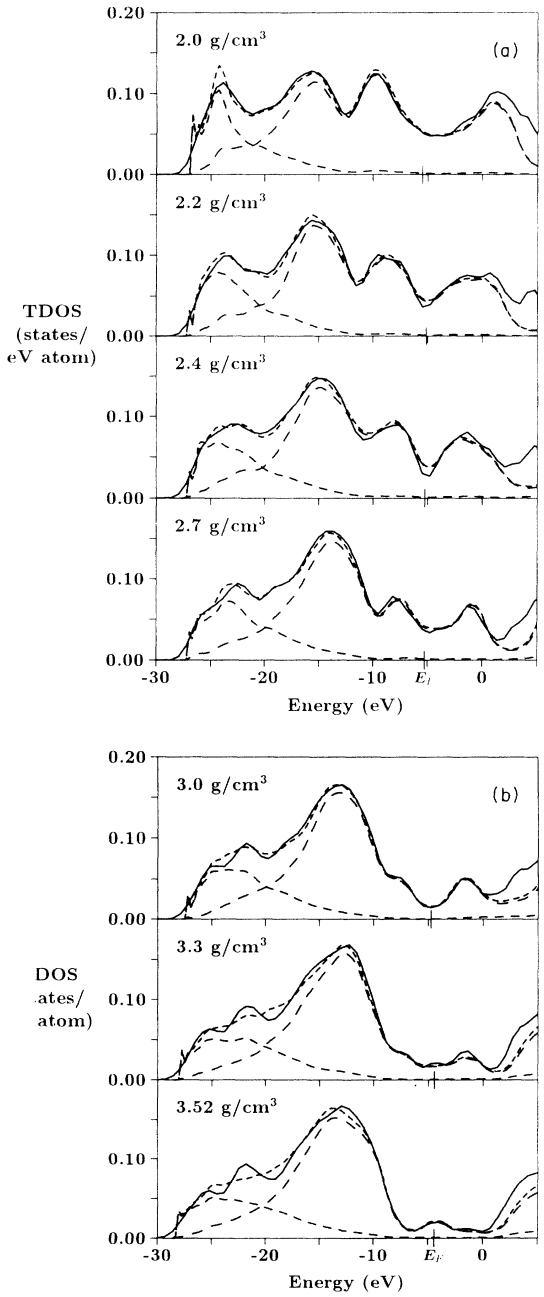


FIG. 3. Total electronic density of states of $a$-C model structures. Solid line, LCAO $\Gamma$-point smoothing; dashed lines, recursion method (short dashes, summed TDOS; medium dashes, $s$ partial TDOS; long dashes, $p$ partial TDOS).

thereby taking into account our $\pi$ bonding analysis of Sec. IV. As seen in Table VI, the number of non-$\sigma$-bonded orbitals decreases continuously with increasing mass density. This orbital number equals the number of states in the $\pi$ part of the TDOS,[20] which therefore is also decreasing. The structure of the $\pi$ band, however, approximately follows from the ratio of the nonbonding to the bonding and antibonding states $n_p/n_\pi$ (see Table VI). For the first three models (2.0–2.4 g/cm$^3$) $n_p/n_\pi$ is very small, which describes the appearance of distinct bonding and antibonding $\pi$ bands enclosing a strong pseudogap. Because this ratio does not differ very much in all three cases, the number of states in the $\pi$ bands and immediately near $E_F$ decreases nearly in the same order. This obviously correlates with the fact that the number of the C3 atoms is nearly constant in these structures, since the enlargement of the C4 fraction is compensated by the diminishing of the C2 atoms. These latter atoms mainly give rise to isolated defects or pairs of $\pi$-bonded orbitals; hence their reduction tentatively decreases the number of defects as well as of the bonding and antibonding states. As a result, which is additionally affected by a partly reverse behavior of the topological defects, a slight decrease in the ratio $n_p/n_\pi$ is observed. Increasing the density above 2.4 g/cm$^3$, the C3 content drops giving rise to a strong further reduction in the bonding and antibonding states, but obviously to a much less variation in the defect density. As a consequence, the relative number of defect states near $E_F$ is now growing. Finally, in the high-density structures defect maxima clearly appear at $E_F$ while the $\pi$ bands tend to vanish. For these structures the relative number of weak $\sigma$ bonds, which are additionally included in our $\pi$-bonding analysis (cf. Sec. IV), is growing as well. This effect leads to an exception from the just stated rule for our 3.0 g/cm$^3$ structure. Here a few weak $\sigma$ bonds are formed which partly saturate a number of otherwise created defect states. The resulting structure is characterized by a very low defect concentration, which indicates the possible stability of such high-density highly tetrahedral amorphous carbon modifications (*ta*-C).

To further clarify this discussion we have depicted the distribution of the size of the $\pi$-bonded clusters in Fig. 4. First of all, one sees a steady decrease in the size of the larger $\pi$ clusters passing from the low- to the high-density structures. This follows from the continuous growing of the C4 content. For the lower-density structures (upper panel of Fig. 4), however, one has also to remember the compensating effect of the C2 decrease which makes the $\pi$ clusters more compact. As stated above, this decrease is additionally reflected by the diminishing of one- and two-atomic $\pi$ groups which are mainly formed by isolated or paired second hybrid orbitals of C2 atoms. After vanishing of the C2 part, the number of C3 atoms decreases leading to a strong further reduction of the cluster size (lower panel of Fig. 4). On the other hand, the number of isolated defects and paired orbitals attains a new maximum which results from the destruction of larger clusters. For the high-density structures, eventually, all $\pi$ clusters become small. In particular, the large relative number of $sp^2$-$sp^2$ pairs, producing double bonds,

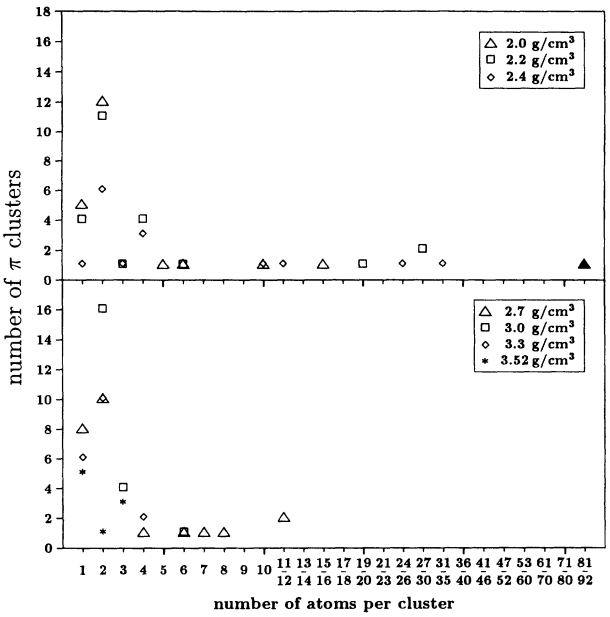


FIG. 4. $\pi$-cluster size distribution in $a$-C models with variation of mass density. (The notation $x/y$ relates to clusters consisting of $x$ up to $y$ atoms. The full triangle denotes a percolating $\pi$ cluster.)

and the complete missing of isolated unbonded orbitals in the 3.0 g/cm$^3$ structure again support the good electronic quality of this material.

Keeping these results in mind, we have investigated the average nearest-neighbor distance between undercoordinated atoms (Fig. 5, solid line) in correlation with the mean values of the overlap integrals between neighboring unsaturated orbitals. The break from the C2 to the C3 decrease can also be seen here. In the first three structures the reduction in the C2 content leads to a saturation of the second free orbitals of these atoms and, consequently, to a diminishing of very short triplelike bonds (cf. the bond-length distribution in Fig. 2). The average distance, therefore, grows to a maximum at 2.4 g/cm$^3$

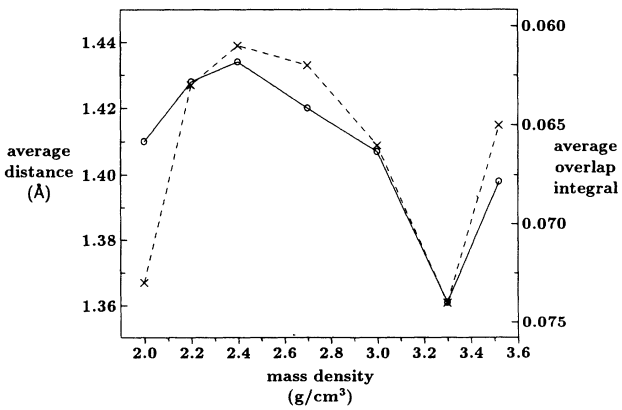


FIG. 5. Correlation between mean nearest-neighbor distances of undercoordinated atoms (solid line) and mean values of overlap integrals between unsaturated orbitals (dashed line) as a function of mass density.

where the minimum of the relative number of two-orbital clusters is reached. (This tendency is described by the values in the last row of Table I.) Related to this behavior, the average overlap integral attains its minimum. Increasing the density further now gives rise to a growing of the relative number of $sp^2$-$sp^2$ double bonds, which becomes maximum at 3.0 and 3.3 g/cm$^3$. For that reason, the average distance drops to its minimum. This fact corresponds with the maximum overlap thus indicating that smaller $\pi$ clusters distributed in the $sp^3$ matrix are able to form strong $\pi$ bonds as the result of minimizing the stress in such systems. Finally, our diamond-density structure is characterized by a high relative number of isolated and topological defects (three-atomic $\pi$ clusters) which again change the slope of the curves. The remarkable correlation found between the average distance and the mean overlap integral is a consequence of the similar angle distributions between unsaturated orbitals in all structures, which because of the $\pi$ interaction is peaked at 0° (and 180°).

We are now in a position to return to our total densities of states in Fig. 3 discussing the gaps between $\pi$ states in more detail. In Fig. 6 we have depicted the separation between the Fermi energy $E_F$ and the maximum of the bonding $\pi$ band $E_\pi^{\max}$ (dashed line) as well as between $E_F$ and the highest occupied $\pi$ level $E_\pi^{\mathrm{HOMO}}$ (solid line). This latter state has approximately been determined by counting down half of the nonbonding states from $E_F$. The different clustering behavior at different densities is again reflected in this diagram. First, we discuss the consequences of the decreasing cluster size going from the low- to the high-density structures. Since the $\pi$ clusters in our models only contain very few rings, their topology is essentially quasilinear. (This term corresponds to the cluster description in the drop model of the percolation theory thinking of clusters with ramification 1.[40,41]) Within such topologies the decreasing cluster size yields a narrowing of the separation between $E_F$ and $E_\pi^{\max}$. On the other hand, larger clusters in general have smaller HOMO-LUMO gaps, a fact which drives the $E_F - E_\pi^{\mathrm{HOMO}}$ value to increase in the given succession of densities.

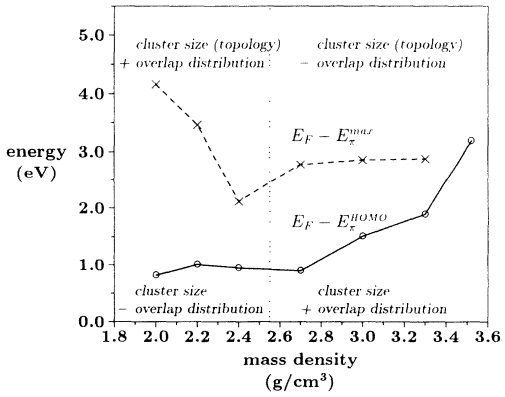


FIG. 6. Variation of energetic separation between $E_F$ and the maximum of the bonding $\pi$ band (dashed line) and between $E_F$ and the highest occupied $\pi$ level (solid line).

Now these effects are superimposed by the changes in the overlap integral distribution, which originates from the aforementioned distance distribution between undercoordinated atoms; cf. Fig. 5. For the lower-density structures up to 2.4 g/cm$^3$ the overlap distribution has increasing weights on smaller overlap integrals which affects both curves in Fig. 6 to decline. The cluster size influence on $E_F - E_\pi^{\max}$ is therefore strengthened, but partly compensated for $E_F - E_\pi^{\mathrm{HOMO}}$. Considering the higher-density structures up to 3.3 g/cm$^3$, this effect reverses because the overlap distribution tends to make both curves in Fig. 6 increase. In this situation the effect of the decreasing cluster size is supported on $E_F - E_\pi^{\mathrm{HOMO}}$, but almost compensated on $E_F - E_\pi^{\max}$.

Summarizing this discussion, the lower-density structures are characterized by a strong decrease of the separation between the maxima of the $\pi$ bands, whereas in the higher-density structures the HOMO-LUMO $\pi$ gap increases. These gaps, given for comparison in Table I, attain maximum values $\gtrsim 3$ eV. Accompanied by a very low defect concentration, the 3.0 g/cm$^3$ structure forms one of the minimal-energy configurations of the models considered. This is in agreement with recent experimental results on *ta*-C thin film structures[2,6,28] and verifies the stability and high $sp^3$ fraction of these materials, hence becoming promising candidates for doping and electronic applications. As the main sources that determine the large band gap in *ta*-C, the $\pi$-bonding cluster size reduction with increasing density (cf. Fig. 4) and the ability of the $\pi$ bonds to highly relax under the constraint of the rigid bonding environment have to be regarded as two supporting mechanisms. The dominating part of the $\pi$ clusters in the 3.0 and 3.3 g/cm$^3$ *ta*-C structures is formed by $sp^2$ pairs which causes both curves in Fig. 6 to approach. The diamond-density structure, on the other hand, is dominated by isolated defects and a few three-atomic clusters that produce a very large $\pi - \pi^*$ gap (Table I), but also a relatively high defect concentration. The total depletion of the $\pi$ states, however, overcompensates the growing of the defects causing this structure to be the minimal-energy modification of the present work.

## VI. LOCAL ELECTRONIC DENSITIES OF STATES

The $\pi$-bonding analysis of Sec. IV is based on the assumption that the essential contributions of the atoms to the total density of states near $E_F$ may be estimated by the topology of $\pi$-like bonded clusters, the bonds of which exceed a critical overlap of the basic free hybrid orbitals. The states at $E_F$ are classified either according to the isolated occurrence of such orbitals as isolated defects which only slightly interact with neighboring hybrids or they are topological defects originating from nonbonding states of at least three-atomic clusters.

To verify these assumptions, we have calculated the local densities of states at numerous atoms of the structures. These calculations were performed by means of the recursion or continued-fraction method, which was already used in Sec. V to determine the TDOS of the

models. The LDOS projected on some chosen atomiclike orbital $|\varphi_\mu\rangle$,

$$n_\mu(E) = \sum_i |\langle\varphi_\mu|\psi_i\rangle|^2 \delta(E-\varepsilon_i)$$
$$= -\frac{1}{\pi}\mathrm{Im}\langle\varphi_\mu|(E-\hat{H})^{-1}|\varphi_\mu\rangle$$

(sum over all eigenstates $|\psi_i\rangle$ with eigenvalues $\varepsilon_i$), is derived by setting the starting orbital of the recursion equal to $|\varphi_\mu\rangle$. For a sufficiently accurate LDOS picture we again applied the Gaussian quadrature approach[39] using 50 recursion levels and 1000 special **k** points.

In Figs. 7–10 we give examples of these calculations for various representative atoms. These results agree with and supplement our previous study.[20] Let us start our discussion with certain C3 atoms which possess one free orbital to participate in $\pi$-like bonds. The atom in Fig. 7(a) does not contribute to any such bond because it is only surrounded by C4 atoms leading to negligible overlap to other free hybrids (the maximum overlap here is 0.001, $p$ character 100%). This atom represents an ideally isolated $p$ defect. On the other hand, a sufficiently well-relaxed "doublelike" bond with overlap (0.076) near the center of the $\pi$-overlap distribution is shown in Fig. 7(b). In spite of the rather distorted local geometry giving rise to one $sp^x$ free hybrid at the calculated atom and one $p$-like orbital at the neighboring site ($p$ characters 86% and 93%), this isolated bond produces clearly separated bonding and antibonding states at both atoms of the bond. An analogous picture can be seen in Fig. 7(c), but this LDOS provides an example for an atom that participates in a weak $\sigma$ bond (the bond length is 1.97 Å; see Sec. IV). Here the formation of an ordinary bond has not been favored because of the strong local distortion that would emerge closing a four-membered ring. In other cases, there are higher-membered rings which tend to close over the weak bond. Considering Figs. 7(b) and 7(c), there is no qualitative difference between the gap regions of both figures apart from a somewhat larger bonding-antibonding separation in the latter LDOS due to the stronger overlap (0.104).

Figure 8 exhibits the simplest case of a cluster that produces a topological $\pi$ defect: the three-atomic $\pi$-bonded chain. For nearly equal energies of the atomic free hybrids a defect state appears that is centered at the two outermost atoms. Hence this defect can be seen in the LDOS at these latter atoms [Fig. 8(b)], but not in the LDOS at the center of the chain [Fig. 8(a)]. A more complicated example of atoms that interact with very different strength is given in Fig. 8(c). By our definition of $\pi$ bonds, the atom in this picture is considered as isolated giving rise to the strong peak at $E_F$. The overlap to one isolated neighboring atom (0.030) is somewhat below our limiting value for $\pi$ bonds. The peak therefore slightly splits into two components. Additionally, there is a second neighboring atom (overlap 0.041) being a member of a strong double bond. The tails of the states related to this bond, slightly enhanced by the weak four-atomic configuration, are clearly seen beside the central peak in Fig. 8(c).

The LDOS pictures in Fig. 9 describe the interesting case of a five-atomic chain with additional triplelike bonds at the ends of the chain. First of all, there is a topological defect having weights at the central and the outermost atoms. The C3 atom at the center, however, possesses a free $sp^x$ (here $sp^{2.38}$) hybrid with very large (30%) $s$ character, which is indicated by the large $s$ part of the peak at $E_F$ in Fig. 9(a). All other atoms of the chain are twofold coordinated. The bonding and antibonding $\pi$-like states at these atoms are therefore aug-

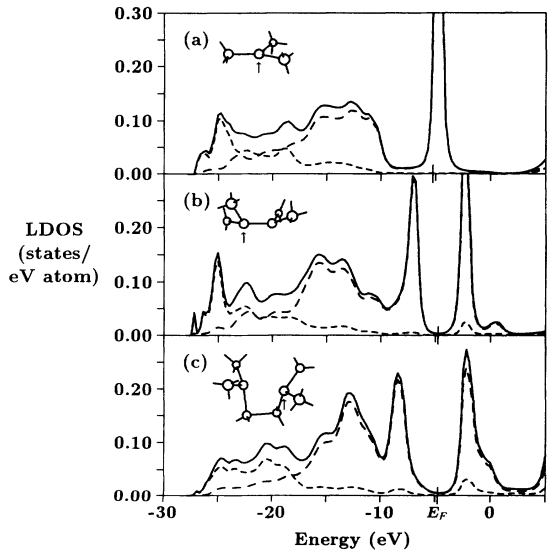


FIG. 7. Local densities of states for selected C3 atoms (short-dashed curve, $s$ partial LDOS; long-dashed curve, $p$ partial LDOS). The arrangement of neighboring atoms around the calculated atom, which is indicated by an arrow, is also sketched in each panel.

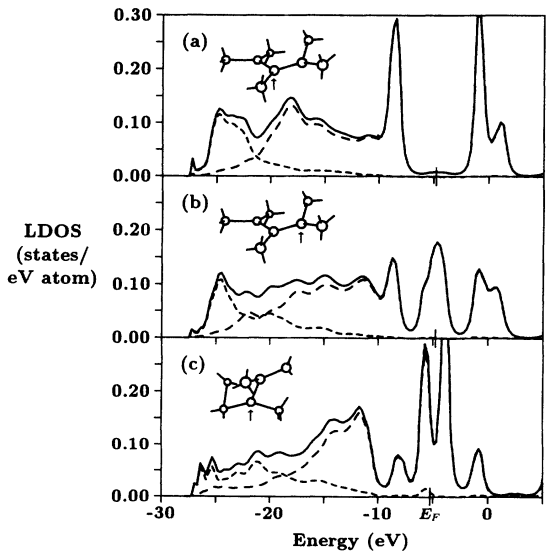


FIG. 8. Local densities of states for selected C3 atoms. The meaning of the dashed curves and of the local-geometry sketches is the same as in Fig. 7.

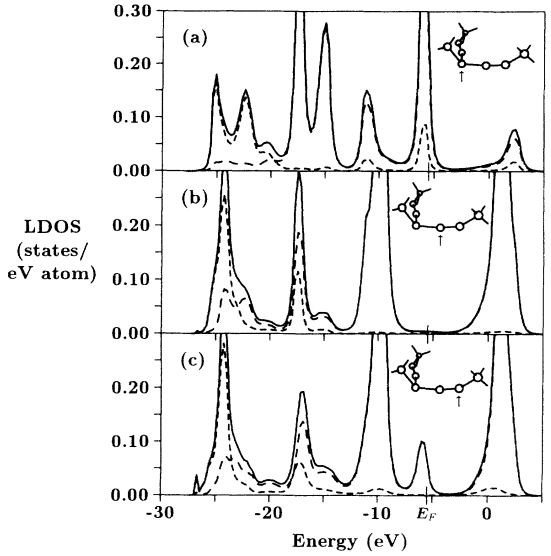


FIG. 9. Local densities of states for selected C3 atoms. The meaning of the dashed curves and of the local-geometry sketches is the same as in Fig. 7.

mented by the superposition of delocalized chain states and other more localized states created by the second free hybrid orbitals [Figs. 9(b) and 9(c)].

For the sake of completeness, let us briefly discuss examples of C2 and C4 atoms. In the upper panel of Fig. 10 we have chosen a C2 atom which is only $\pi$-like bonded by its free pure $p$ orbital. This orbital contributes to a $\pi$ cluster in an analogous way as described for the C3 atoms. In our case, the bonding and antibonding states near $E_F$ are created. The unbonded hybrid orbital ($sp^{2.19}$, 31% $s$) produces, however, the sharp peak at $E_F$, which again is characterized by a very large $s$

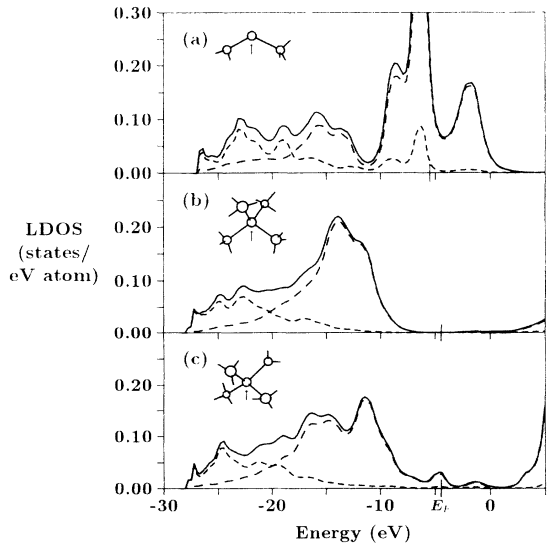


FIG. 10. Local densities of states for a C2 (a) and two C4 atoms. The meaning of the dashed curves and of the local-geometry sketches is the same as in Fig. 7.

part. C4 atoms, on the other hand, attain a formally complete chemical bond saturation and, in general, produce a distinct minimum LDOS region around $E_F$. Figure 10(b) shows a well-relaxed atom (standard deviation of the bond angles $\Delta\varphi = 4.3°$ and of the bond lengths $\Delta r = 0.019$ Å). With increasing deviations from the diamondlike short-range order, however, and additionally affected by interactions with free orbitals of neighboring atoms, the maximum of the $\sigma$ valence band often shifts to higher energies and the gap region fills by tails and certain small peaks [Fig. 10(c): $\Delta\varphi = 14.2°, \Delta r = 0.058$ Å]. These results agree with earlier tight-binding investigations on the effects of bond-length, bond-angle, as well as dihedral-angle disorder,[42] and with recent calculations on fourfold-coordinated random network models[43] for which a notable density of states has emerged in the gap region with increasing off-diagonal disorder.

## VII. CONCLUSION

We have applied a semiempirical molecular-dynamics density-functional approach for investigation of the atomic as well as electronic structure of amorphous carbon $a$-C systems. The models with mass densities exceeding 3.0 g/cm$^3$ have been determined to be the most stable modifications under the given set of simulation conditions. These density values in correspondence with high fractions of $sp^3$ bonded carbon atoms (64–88%), are close to the results for highly tetrahedral amorphous carbon $ta$-C, obtained experimentally by vacuum arc and mass-selected ion beam deposition.[1–5] Though some experiments[2] report on higher $sp^3$ fractions even for structures of about 3.0 g/cm$^3$ (cf. Table III), theoretically simulated diffraction data compared with electron diffraction results[28] suggest that the theoretically obtained lower values are probably more realistic to describe the deposited films correctly.

As an important characteristic affecting the stability of the generated models, the electronic density of states behavior within the gap region has been discussed in terms of global electronic parameters such as the HOMO-LUMO $\pi - \pi^*$ band gap and the relative weight of the defect states. These properties are controlled by the size and topology of various $\pi$-bonded clusters which have been investigated by a simple $\pi$-bonding analysis. Whereas the $\pi$ clusters at the lowest mass density percolate through the system forming the matrix with incorporation of cross-linking $sp^3$ sites, the smaller clusters at densities $\geq 3.0$ g/cm$^3$ are embedded within the rigid $sp^3$ bonding environment. The stress in these high-density amorphous networks is reduced by the preferred formation of $\pi$ bonded $sp^2$ pairs giving rise to maximum mean $p$-orbital overlap values. As a consequence, in these models being in agreement with experimental results large $\pi - \pi^*$ band gaps of about 3 eV are created. Moreover, the 3.0 g/cm$^3$ model is additionally characterized by the lowest number of defects. This is very hopeful for future doping investigations and verifies the structural and electronic stability of such films. On the other hand, no substantial aromatic clustering has been observed at any density.

The defect states near $E_F$ have been classified according to their molecular formation as isolated defects or topological ones. A striking feature which strongly influences the defect creation within our low-density structures is the relatively high number of twofold coordinated atoms. Investigations based upon an improved and more extended relaxation scheme give evidence of a reduction of this C2 part. These calculations are now in progress.[44]

Coordinates of the models discussed in this paper are available upon request.[45]

## ACKNOWLEDGMENTS

We gratefully acknowledge the financial support from the Deutsche Forschungsgemeinschaft. We would like to thank M. Weiler, H. Ehrhardt, K. Jung (Kaiserslautern), V. S. Veerasamy, G. A. J. Amaratunga (Cambridge), and W. R. L. Lambrecht (Cleveland) for stimulating discussions.

[1] I. I. Aksenov, S. I. Vakula, V. G. Padalka, R. E. Strelnitzki, and V. M. Khoroshikh, Sov. Phys. Tech. Phys. **25**, 1164 (1980).
[2] D. R. McKenzie, D. Muller, and B. A. Pailthorpe, Phys. Rev. Lett. **67**, 773 (1991).
[3] J. Ishikawa, Y. Takeiri, K. Ogawa, and T. Tagaki, J. Appl. Phys. **61**, 2509 (1987).
[4] J. Koskinen, J. Appl. Phys. **63**, 2094 (1988).
[5] Y. Lifshitz, S. R. Kasi, and J. W. Rabalais, Phys. Rev. Lett. **68**, 620 (1989).
[6] V. S. Veerasamy, G. A. J. Amaratunga, W. I. Milne, P. Hewitt, P. J. Fallon, D. R. McKenzie, and C. A. Davis, Diamond Relat. Mater. **2**, 782 (1993).
[7] V. S. Veerasamy, G. A. J. Amaratunga, C. A. Davis, A. E. Timbs, W. I. Milne, and D. R. McKenzie, J. Phys. Condens. Matter **5**, L169 (1993).
[8] C. A. Davis, D. R. McKenzie, Y. Yin, E. Kravtchinskaia, G. A. J. Amaratunga, and V. S. Veerasamy, Philos. Mag. B (to be published).
[9] D. R. McKenzie, Proceedings of the International Conference on Amorphous Semiconductors, Cambridge, England, 1993 [J. Non-Cryst. Solids (to be published)].
[10] J. C. Angus and F. Jansen, J. Vac. Sci. Technol. A **6**, 1778 (1988).
[11] J. Robertson, Surf. Coat. Technol. **50**, 185 (1992); Diamond Relat. Mater. **2**, 984 (1993).
[12] G. Galli, R. M. Martin, R. Car, and M. Parrinello, Phys. Rev B **42**, 7470 (1990).
[13] P. Blaudeck, Th. Frauenheim, D. Porezag, G. Seifert, and E. Fromm, J. Phys. Condens. Matter **4**, 6389 (1992).
[14] Th. Frauenheim, P. Blaudeck, U. Stephan, and G. Jungnickel, Phys. Rev. B **48**, 4823 (1993).
[15] P. C. Kelires, Phys. Rev. B **47**, 1829 (1993).
[16] C. Z. Wang, K. M. Ho, and C. T. Chan, Phys. Rev. Lett. **70**, 611 (1993).
[17] D. A. Drabold, P. A. Fedders, and P. Stumm, Phys. Rev. B **49**, 16 415 (1994).
[18] J. Robertson and E. P. O'Reilly, Phys. Rev. B **35**, 2946 (1987).
[19] J. Robertson, Diamond Films Conference, Albufeira, 1993 [Diamond Relat. Mater. (to be published)].
[20] U. Stephan and M. Haase, J. Phys. Condens. Matter **5**, 9157 (1993).
[21] Ch. Lee, W. Lambrecht, B. Segall, P. Kelires, Th. Frauenheim, and U. Stephan, Phys. Rev. B **49**, 11 448 (1994).
[22] Th. Frauenheim, G. Jungnickel, U. Stephan, P. Blaudeck, S. Deutschmann, M. Weiler, S. Sattel, K. Jung, and H. Ehrhardt, Phys. Rev. B (to be published).
[23] G. Seifert, H. Eschrig, and W. Biegert, Z. Phys. Chem. (Leipzig) **267**, 529 (1986).
[24] G. Seifert and R. O. Jones, Z. Phys. D **20**, 77 (1991).
[25] P. Blaudeck, Th. Frauenheim, H.-G. Busmann, and Th. Lill, Phys. Rev. B (to be published).
[26] Th. Frauenheim, U. Stephan, P. Blaudeck, D. Porezag, H.-G. Busmann, W. Zimmermann-Edling, and S. Lauer, Phys. Rev. B **48**, 18 189 (1993).
[27] M. Weiler, R. Kleber, S. Sattel, K. Jung, H. Ehrhardt, G. Jungnickel, S. Deutschmann, U. Stephan, P. Blaudeck, and Th. Frauenheim, Diamond Relat. Mater. **3**, 245 (1994).
[28] G. Jungnickel, M. Kühn, S. Deutschmann, F. Richter, U. Stephan, P. Blaudeck, and Th. Frauenheim, Diamond Relat. Mater. (to be published).
[29] G. Jungnickel, Th. Köhler, M. Haase, U. Stephan, S. Deutschmann, P. Blaudeck, and Th. Frauenheim, J. Non-Cryst. Solids (to be published).
[30] F. Li and J. S. Lannin, Phys. Rev. Lett. **65**, 1905 (1990); H. Pan, M. Pruski, B. C. Gerstein, F. Li, and J. S. Lannin, Phys. Rev. B **44**, 6741 (1991).
[31] M. Heggie, J. Phys. Condens. Matter **3**, 3065 (1991).
[32] M. Stutzmann, Philos. Mag. B **56**, 63 (1987); **60**, 531 (1989).
[33] Rui-qin Zhang, Solid State Commun. **69**, 681 (1989).
[34] W. B. Jackson, Phys. Rev. B **41**, 10 257 (1990).
[35] V. Heine, D. W. Bullett, R. Haydock, and M. J. Kelly, *Solid State Physics* (Academic, New York, 1980), Vol. 35.
[36] H. J. Monkhorst and J. D. Pack, Phys. Rev. B **13**, 5188 (1976).
[37] S. M. Anlage and D. L. Smith, Phys. Rev. B **34**, 2336 (1986).
[38] M. Krajči, J. Phys. F **17**, 2217 (1987).
[39] C. M. M. Nex, J. Phys. A **11**, 653 (1978).
[40] A. Coniglio, Phys. Rev. Lett. **46**, 256 (1981).
[41] Y. Gefen, A. Aharony, B. B. Mandelbrot, and S. Kirkpatrick, Phys. Rev. Lett. **47**, 1771 (1981).
[42] J. Singh, Phys. Rev. B **23**, 4156 (1981).
[43] T. Koslowski and W. von Niessen, J. Phys.: Condens. Matter **4**, 6109 (1992).
[44] Th. Köhler, M. Haase, G. Jungnickel, U. Stephan, and Th. Frauenheim (unpublished).
[45] Please direct requests to frauenheim@physik.tu-chemnitz.de

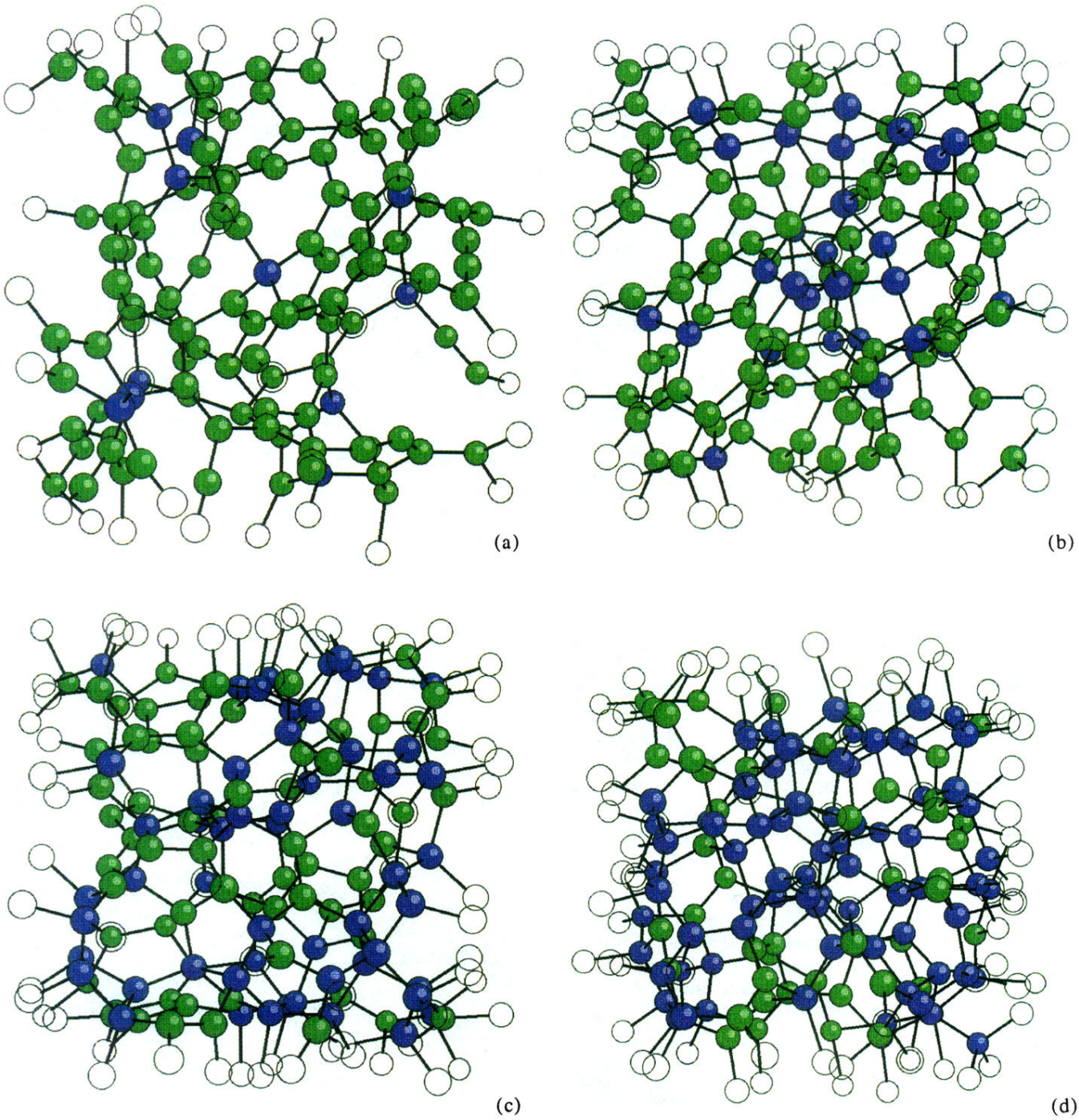


FIG. 1. Computer images of $a$-C supercell structures with variation of mass density: 2.0 (a), 2.4 (b), 2.7 (c), 3.0 (d), 3.3 (e), and 3.52 g/cm$^3$ (f). Green spheres denote twofold and threefold coordinated atoms, blue spheres denote fourfold ones. Open circles refer to atoms in the neighboring supercells. For convenience (e) and (f) have been enlarged as compared with the first ones by a factor of 65/60.

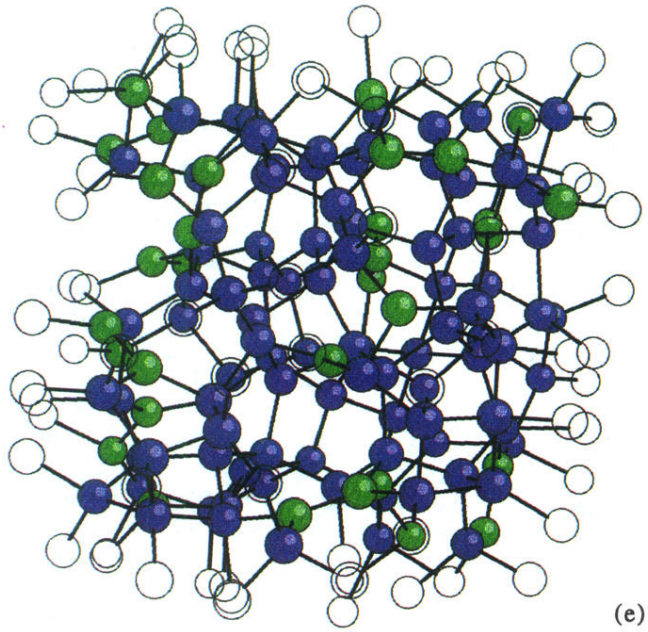

(e)

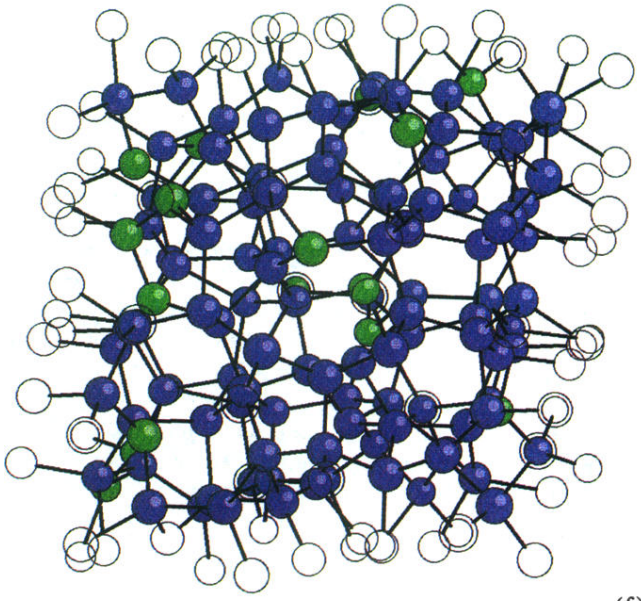

(f)

FIG. 1 *(Continued).*

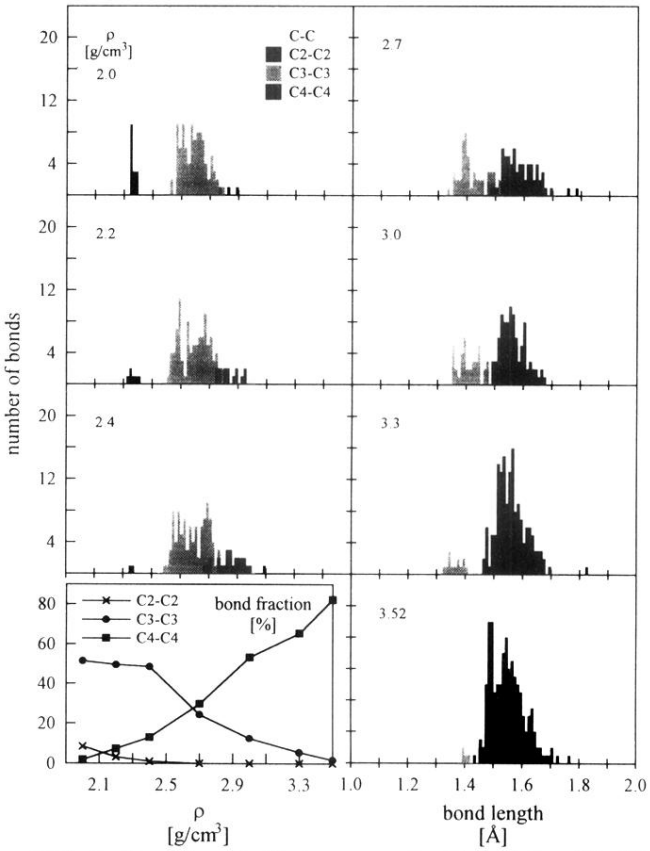


FIG. 2. Bond-length histograms of $a$-C models with different mass densities $\rho$. Furthermore, the fractions of C2-C2, C3-C3, and C4-C4 bonds related to all bonds within the models are also shown.